Predicting the Onset of Dynamic Stall on Large Wind Turbines

Jan Dominik Ahrens, Jasson A. Printezis, Ahmed G. Yosry, Joerg R. Seume, and Lars Wein

Leibniz University Hannover: Institute of Turbomachinery and Fluid Dynamics, An der Universitaet 1, 30823 Garbsen

Correspondence: wein@tfd.uni-hannover.de

Abstract.

This study addresses the challenge of predicting dynamic stall on wind turbine airfoils, focusing on the development of a reduced-order model applicable to thick airfoils (t/c > 0.21). Utilizing a Delayed Detached-Eddy simulation of a pitching FFA-W3-211 airfoil at Re = 15 M, our analysis identifies the transition from the primary instability phase to the vortex formation stage as a critical aspect of dynamic stall. By examining the dynamic time scales, we observed a ten-fold increase in the growth rate of the shear layer height during the transition of these stages. The stall delays attributed to these stages are substantially dependent on the airfoil's camber distribution and the location of the maximum thickness. We discovered that the Leading-Edge Suction-Parameter (LESP) proposed by Ramesh et al. (2014) for thin airfoils is also helpful in predicting the onset of the vortex formation stage for thick airfoils. Based on this finding, we propose a Mid-Chord Suction-Parameter (MCSP), that is more effective for wind turbine airfoils. The MCSP exhibits a breakdown in magnitude at the onset of the vortex formation stage and deep stall.

1 Introduction

Wind turbines (WTs) generate power based on the square of their rotor diameter, driving the trend towards larger WTs. The next generation of offshore megastructures will reach rated capacities of approx. 20 MW and diameters of 350 m. The elongated and flexible rotor blades of these megastructures are more prone to deformations, which, along with wind speed fluctuations, turbulence, and altitude-dependent wind distribution, locally alter the blade's angle of attack (AoA). If the AoA exceeds the static stall angle, it can trigger dynamic stall. Dynamic stall introduces transient loads that excite blade vibrations, which contribute to mechanical fatigue and can lead to blade failure. It is, therefore, crucial to predict the onset of dynamic stall and account for the increased dynamic loads in the design of future WT blades. Dynamic stall has long been a subject of research in helicopter aerodynamics (Leishman, 2006; Corke and Thomas, 2015). It has been investigated through both experiments, such as those conducted by Merz et al. (2017) and Schwermer et al. (2019), and computational fluid dynamics (CFD), as demonstrated by Letzgus et al. (2019). Differences between dynamic stall on helicopter and WT blades are the larger diameters and chord

25   lengths, resulting in higher Reynolds numbers (Re ≈ 15M) and lower Mach numbers (Ma < 0.3). Additionally, WT
     airfoils have a higher thickness-to-chord ratio of t/c > 0.21 and Bangga et al. (2017) has shown that the flow around
     WT blades can be assumed quasi-three-dimensional (Q3D) for regions outside of the inner 30% of the span. In their
     work, Sharma and Visbal (2019) investigated the influence of airfoil thickness on dynamic stall and found that the
     role of trailing-edge separation increases with thickness. They noted that for Q3D simulations, a span of 10% of

30   the chord is sufficient to study the onset of dynamic stall. The stall behaviour of an airfoil gradually shifts from
     trailing-edge stall to leading-edge stall and the stall angle and maximum lift increase for growing Reynolds numbers
     above 2 M Brunner et al. (2021). Kiefer et al. (2022) found that for thick airfoils as they occur on WTs, the stall
     delay is characterised by a power law that is a function of the Reynolds number, kinematics of the pitching motion,
     and airfoil geometry parameters. An airfoil is assumed to be thick for a thickness-to-chord-ratio t/c > 0.21. Huang

35   et al. (2020) identified the freestream's turbulence as a critical parameter that delays the onset of dynamic stall.
     The higher the freestream's turbulence, the later the dynamic stall vortex forms. The three stages of dynamic stall
     according to Mulleners et al. (2012) are the primary instability stage, vortex formation stage, and deep stall. When
     exceeding the static stall angle α_{SS}, the boundary layer enters the primary instability stage, which is characterized
     by the formation of small eddies on the suction side of the airfoil and an increase in lift above the maximum of

40   the static case. Further increasing the angle of attack above α_* initiates the vortex formation stage. The unstable
     boundary layer rolls up and the dynamic stall vortex is formed. This vortex subsequently detaches and the airfoil
     reaches deep stall, which leads to a sudden drop in the lift. Decreasing the angle of attack prior to exceeding α_*,
     prevents the formation of a dynamic stall vortex and keeps the airfoil in the light stall regime, which is associated
     with significantly lower dynamic blade loads and load oscillations (Mulleners et al., 2012; Deparday and Mulleners,

45   2019). The total stall delay is composed of the stall delay attributed to the primary instability stage Δt_1^* and the
     stall delay attributed to the vortex formation stage Δt_2^*. Δt_1^* is a function of the airfoil geometry and unsteadiness
     of the flow, whereas Δt_2^* depends on the freestream's conditions (Mulleners et al., 2012; Kiefer et al., 2022).
     The operating conditions of WTs are highly unsteady and vary over span of the blades. Preventing the local angle
     of attack from exceeding the static stall angle at every span-wise position and, thereby, avoiding dynamic stall

50   is an impossible task with global pitch control. Changing the pitch angle locally would require expensive gear
     that measures the local angle of attack at multiple span-wise positions and an approach to locally reduce that
     angle of attack. Gerontakos and Lee (2006) and Andersen et al. (2009) investigated trailing-edge flaps as a way
     to avoid dynamic stall. However, installing according devices in a WT would drastically increase the cost and the
     maintenance intervals. A cost-effective way of mitigating the effects of dynamic stall is to develop airfoil geometries

55   that are inherently less prone to dynamic stall. In order to design such airfoils, α_* (Δt_1^*) has to be predicted and
     maximized for the new airfoil designs. This is possible because Δt_1^* is a function of the airfoil geometry. However,
     current dynamic stall models like the Blade Element Momentum (BEM) method only predict the dynamic loads and
     cannot predict the time scales of dynamic stall (Branlard et al., 2022). Additionally, dynamic stall models that are
     based on the BEM method require empirical results and rely on parameters that are derived from the static lift curve

60 of already existing airfoils. These lift curves have to be obtained via expensive experiments or CFD simulations and are acquired for every combination of airfoil geometry and aerodynamic boundary conditions that are investigated in the BEM simulation. Applying these empirical results to new airfoil geometries leads to large uncertainties in the BEM simulations (Tangler, 2002; Simms et al., 2001). This demonstrates the need for a non-empirical ROM for predicting the onset of the vortex formation stage. An example for such an approach for thin airfoils was established

65 by Ramesh et al. (2014) who introduced the critical leading-edge suction parameter (LESP_crit), which is a criterion for intermittent vortex shedding. The LESP is a measure of the suction at the leading edge and is calculated by integrating the lift at the airfoil wall in the interval $0 < x/c < 0.1$ and normalizing it with the dynamic pressure at the inlet $0.5\rho U_\infty^2$. They found that for any thin airfoil and Reynolds number, there exists a critical LESP_crit. When exceeded, vortex shedding occurs at the leading-edge marked by a sudden breakdown of the suction of the airfoil.

70 The temporal evolution of the LESP can be predicted by reduced-order models that calculate an unsteady pressure distribution around the airfoil (e.g. unsteady vortex-lattice method (Konstadinopoulos et al., 1985)). LESP_crit is a function of the airfoil geometry and Reynolds number and using thin airfoil theory, we can predict it with the first term of the Fourier series of the vortex sheet strength distribution along the camber line. Using this relationship, Deparday and Mulleners (2019) predicted the onset of the vortex formation stage for thin airfoils based on LESP_crit

75 and improved the method by introducing an effective angle of attack that depends on the instantaneous shear layer height at the suction side of the airfoil. Mulleners et al. (2012), Gupta and Ansell (2019), and Sharma and Visbal (2019) state, that for thick airfoils the dynamic stall vortex does not form at the leading-edge but at mid-chord. This was experimentally confirmed by Kiefer et al. (2022). Based on these observations, we hypothesize that there exists a critical mid-chord suction parameter (MCSP_crit) for thick airfoils that indicates the formation of the dynamic stall

80 vortex. The MCSP is a measure of the suction at mid-chord and is calculated by integrating the lift at the airfoil wall in the interval $0.45 < x/c < 0.55$ and normalizing it with the dynamic pressure at the inlet. Both the LESP_crit and MCSP_crit are criteria that predict vortex shedding without relying on empirical static polars like the BEM method. We test our hypothesis by conducting a Delayed Detached-Eddy simulation (DDES) of dynamic stall at a Reynolds number of 15 M. This Reynolds number will be reached by future offshore WTs and, to the knowledge of

85 the authors, dynamic stall has not been investigated at such operating conditions with scale-resolving simulations.

2 Methodology

2.1 Delayed Detached-Eddy simulation

OpenFOAM v2012, an open-source CFD software, is used to run a three-dimensional transient DDES simulation for investigating dynamic stall on the FFA-W3-211 airfoil (Fig. 6). The FFA-W3-211 airfoil is a commonly used geometry

90 for WTs with a height-to-chord ratio of 21.1% and the coordinates of the geometry can be found in Bertagnolio et al. (2001). The main purpose is to predict the flow separation on the suction side of the airfoil for both the static and the dynamic case at a Reynolds number of 15 M, which is representative for future offshore WTs.

The computational domain is presented in Fig. 1. It is a cylinder with a diameter of $50 \times c$ and a length of $1 \times c$ in span-wise direction, whereas c is the chord length of the airfoil. These dimensions have been successfully used by Yalcin
95   et al. (2021) to obtain simulation results that are independent of the far-field and the span-wise mesh resolution, allowing for an analysis of the flow phenomena around airfoil. The boundary conditions for the computational domain at hand are summarized in Tab. 1. At the inlet, a uniform velocity and a zero gradient for the kinematic pressure are applied, while a zero gradient for the velocity and a uniform kinematic pressure of $p/\rho = 0$ (incompressible flow) is applied at the outlet. A symmetry condition is used for all wall boundaries, except for the airfoil surface, where a
100 zero-velocity condition is enforced. The pitching motion of the airfoil is implemented via a sliding mesh approach, which we have successfully implemented for investigating dynamic stall in Ahrens et al. (2022). The approach keeps the two meshes (the domain and the airfoil) connected during the transient pitching motion via interpolation of the flow quantities.

Table 1. Initial and boundary conditions

Boundary	$U_\infty, [m/s]$	$p/\rho, [m^2/s^2]$	$k, [m^2/s^2]$	$\omega, [1/s^2]$	$nut, [m^2/s]$
Inlet	fixedValue, U_∞	zeroGradient	$I_t = 0.05$	$L_{mixing} = 0.2625$	calculated
Outlet	zeroGradient	fixedValue, 0	inletOutlet	inletOutlet	calculated
AMI	cyclicAMI	cyclicAMI	cyclicAMI	cyclicAMI	cyclicAMI
Airfoil	movingWallVelocity	zeroGradient	fixedValue, $1e-9$	omegaWallFunction	nutlowReWallFunction
Walls [sides]	symmetry	symmetry	symmetry	symmetry	symmetry
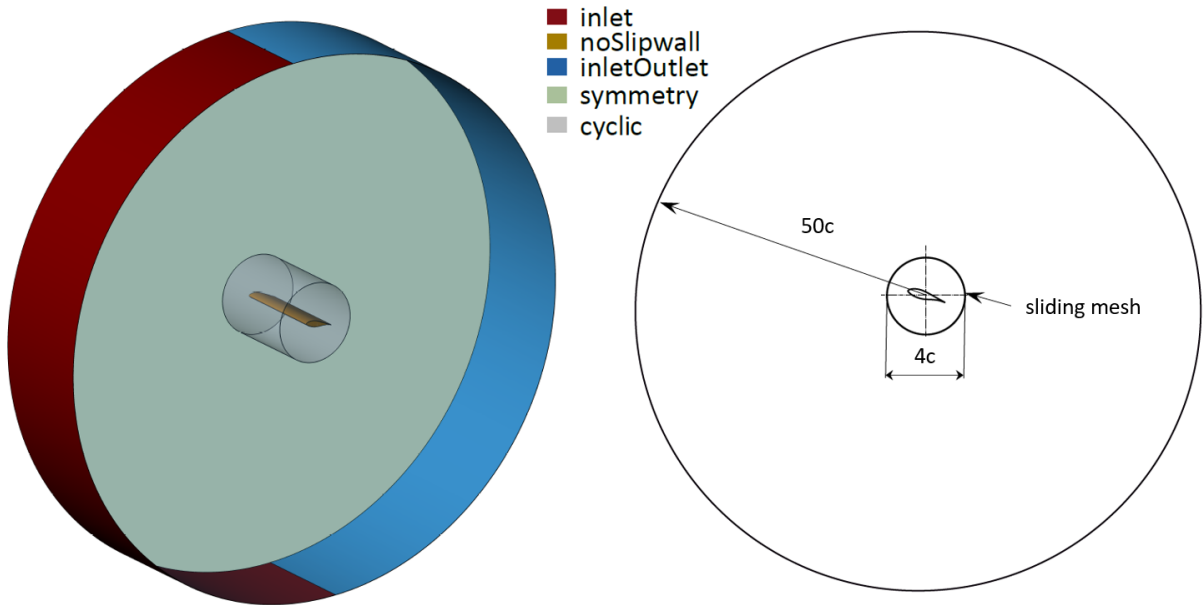
Figure 1. The boundary conditions and dimensions of the computational domain used to simulate static and dynamic stall.

The initial values for all internal fields are estimated with the inlet velocity, the chosen turbulence model, the

105   hydraulic diameter and the Turbulence Intensity (TI = 0.1%). As in Solomin and Ryavkin (2023), the two-equation shear stress transport (k-ω SST) model provides turbulence closure for three-dimensional Reynolds-averaged Navier-Stokes equations (RANS) in the attached flow regions of the DDES simulations. The transient and incompressible pimpleFoam solver has been used for the simulations at hand. It uses the PIMPLE (merged PISO-SIMPLE) algo-rithm for the pressure and velocity coupling (Issa, 1986). The correction of dominant fluxes in the impacted cells

110   considers the impact of mesh movement. This correction involves substituting the velocity with a relative velocity in all convection terms. A comprehensive explanation of this process can be found in the reference Jasak (2009). OpenFOAM uses the finite volume (fV) method to discretize the differential RANS equation. The choice of the proper discretization schemes is based on the balance between the accuracy and the stability. The selected schemes for each sub-dictionary in the code are summarized in Tab. 2.

115 ## 2.2   Blade Element Momentum

The most common reduced-order method for predicting dynamic stall with low computational effort is the Blade Element Momentum (BEM) method. The approach of the BEM method to predict aerodynamic loads on WTs has been presented in detail in previous publications and is summarized here for reference (Branlard et al., 2022). The BEM method is a widely adapted approach, which serves to ascertain the aerodynamic characteristics and loads

120   of WT rotor blades. The first attempt using this method was in the 19th century by William Froude and Stefan

Table 2. Numerical schemes of the DDES

Operator	Selected schemes	Accuracy order
ddtSchemes	CrankNicolson, 0.9	90% 2nd + 10% 1st
gradSchemes (∇)	Gauss linear	2nd
divSchemes ($\nabla\cdot$)	bounded Gauss linearUpwind	2nd upwind
laplacianSchemes (∇^2)	Gauss linear limited corrected, 0.5	2nd

Drzewiecki aiming to analyze and calculate global forces of a screw propeller of marine propulsion (van Bussel, 2020). With the help of Betz (1926), who analyzed the maximum possible energy yield of WTs, Glauert (1935) was able to establish the fundamental BEM equations. The BEM method integrates two theories: the momentum theory and the blade element theory. On the one hand, the momentum theory characterizes flow dynamics within a control volume which includes the entire rotor. The simplifications that are assumed in momentum theory are the following:

- Steady, incompressible, and frictionless flow

- Axial symmetric flow

- Abrupt alteration of the pressure at the rotor

- Flow interactions solely with the rotor, disregarding ambient potential flow

The momentum theory is separated in a momentum analysis in wind direction and an angular momentum analysis in rotational direction. Due to these two analyses thrust and torque acting on the rotor can be calculated. On the other hand, the blade element theory divides the WT blade into infinitesimal radial segments, each autonomously responsive to inflow conditions. The momentum analysis is applied to each individual segment. Therefore, the two theories are harmonized by obtaining thrust and torque for individual radial positions of a rotor blade. These forces are then integrated cumulatively over the entire length of the blade to give the global load acting on the entire blade. Prediction of blade loads for a certain airfoil geometry requires, therefore, empirical results for that airfoil. These results can either be acquired experimentally or with computational fluid dynamics (CFD) simulations. To increase the accuracy of BEM models, correction models have been developed over time. These correction models do not change the fundamental calculation algorithm of the BEM theory, but extend it by taking into account additional physical effects. The physical effects that are taken into account by correction models in the development of the BEM model used in this work are as follows:

- Created vortices at the tip of the rotor blades

- Induced velocities for $\alpha > 0.4$

- Skewed wake effect

145   – Dynamic Stall

Firstly, the BEM method ignores the creation of generated vortices at the tip of the rotor blade. The tip vortices have a deteriorating impact at the lift and drag coefficient of the rotor blade. Thus, they lead to a decrease of aerodynamic efficiency for the blade segments near the blade tip. Using the Prandtl tip loss factor developed by Prandtl and Betz (2010) the altered circulation near the blade tip is being considered, enabling a more precise

150   modelling. The second correction model was developed by Glauert (1926) and considers large induced velocities. The fundamental principles of the BEM theory become inapplicable when the axial induction factor a surpasses 0.4, driven by a notable increase in tip speed ratio. Empirical data derived from a helicopter rotor measurement corrects the progression of the rotor thrust for $a > 0.4$. Another correction model takes into account behavior of the wake. The airflow passing through the rotor blades does not move straight through them. Instead, the airflow is

155   twisted and skewed by passing through the blades. This happens because the spinning rotor blades add a rotational component to the axial moving airflow. With the help of the skewed wake correction model developed by Pitt and Peters (1980) the orientation of the wake is corrected.

The most widely applied dynamic stall models in literature for WTs are the Beddoes-Leishman model (BLM) and the Øye's model. The foundation of the Beddoes-Leishman Model (BLM) rests upon calculated static polar

160   information Leishman and Beddoes (1989). According to Simms et al. (2001) and Tangler (2002) the largest source of error in rotor load and performance predictions is suspected to be due to incorrect static polar information. Thus, the quality of a dynamic stall model is largely dependent on the quality of the calculated static polar data.

Gupta and Leishman (2006) divide the BLM into three modules: unsteady attached flow, unsteady separated flow, and vortex lift. The unsteady attached flow module derives from Theodorsen's foundational work (Theodorsen,

165   1935) on unsteady aerodynamic force calculations within fluid flows around objects. The accurate forecast of unsteady aerodynamic forces and moments of attached flows is important for the correct prediction of the dynamic stall effect. Due to a superposition of aerodynamic forces and moments, the BLM calculates the behavior of the unsteady attached flow. The second module addresses detached flow's aerodynamic forces and moments and is the most important in modelling dynamic stall. The module subdivides into the leading edge separation and the trailing

170   edge separation sub-module. The leading edge separation sub-module is modelling flow separation due to a criterion which determines the critical pressure at the leading edge and its corresponding pressure gradient. The critical pressure and its pressure gradient are equivalent to a critical value of the normal coefficient. When the critical normal coefficient is smaller than the critical coefficient subtracted with the delay of the critical pressure, leading edge separation occurs. The trailing edge separation sub-module uses Kirchhoff's theory of a flow around a flat

175   plate to model lift in post-separation. Using the loss of circulation occurring due to dynamic stall, this sub-module calculates the non-linear behavior of lift, drag and pitching moment. The vortex lift module adds the lift generated by the leading edge vortex to the lift determined by the trailing edge module. As a result, the total unsteady lift is calculated (Khan, 2018).

180 This summary illustrates the main disadvantages of the BEM: The need for empirical lift polars and the inability to predict the onset of the vortex formation stage, which makes BEM unfeasible for designing future airfoils with a maximized α^*. In this work, we, therefore, investigate the temporal evolution of the LESP and the introduced MCSP, which both provide the possibility to predict the onset of the vortex formation stage.

2.3 Non-dimensionalization

185 Comparability of the results presented in this paper is ensured by providing non-dimensional flow quantities. The non-dimensional quantities analyzed in this work are listed in the following paragraph. The chord Reynolds number

$$\text{Re} = \frac{c \cdot U_\infty}{\nu} \tag{1}$$

is based on the chord length c, the freestream velocity U_∞, and the kinematic viscosity nu. The non-dimensional cell height at the wall

$$y^+ = \frac{y \cdot \sqrt{\tau_\mathrm{w}/\rho}}{\nu} \tag{2}$$

should not exceed 1 and is calculated with the cell height at the wall y, the wall shear stress τ_w and the density ρ. The lift coefficient is based on the lift force of the airfoil l:

$$c_\mathrm{l} = \frac{l}{\rho U_\infty^2 c} \tag{3}$$

Dynamic stall is induced via a periodical pitching motion. This leads to self intersection of the visualized quantities
195 when both the up-stroke and down-stroke are plotted as a function of the angle of attack. Instead, the dynamic time scales are visualized as a function of the non-dimensional time:

$$t^* = \frac{t \cdot U_\infty}{c} \tag{4}$$

3 Results

In the present work, two cases are defined for investigating dynamic stall at operating conditions of future WTs. In
200 a first step, the flow around the FFA-W3-211 airfoil is simulated at a constant angle of attack and Re = 15 M. This simulation is carried out with 3 different mesh resolutions to determine the necessary resolution for predicting the blade loads. The spatial grid convergence is analyzed as in Steffen et al. (1995) and the mesh with sufficient mesh resolution is then used for the second case. In the second case, the airfoil is pitched around the z-axis at $0.3c$ to induce dynamic stall.

3.1 Mesh Study

The angle of static stall for the considered airfoil and Reynolds number (Re = 15 M) is $\alpha_{ss} \approx 18°$. The angle of attack for the mesh study is, therefore, chosen as $\alpha = 20°$ to ensure separated flow. The structured computational mesh for the finest case is shown in Fig. 2. The number of cells around the airfoil and the resulting non-dimensional cell sizes x^+_{max} for every mesh resolution are listed in Tab. 3. For all tested meshes, $y^+ < 1$ is ensured and a constant growth factor of 1.2 is applied for the remaining cells in the computational domain. The span-wise direction is resolved with 117 cells ($\Delta z = 0.03c$), which corresponds to the span-wise resolution prescribed in Yalcin et al. (2021) to simulate separated flow with DDES.

Table 3. Investigated mesh resolutions in the mesh study.

Mesh Resolution	N cells around airfoil	N total cells	x^+_{max}
Fine	1000	42.7 M	1300
Medium	500	21.2 M	2812
Coarse	250	8.5 M	7000

(a) Leading-edge.   (b) Trailing-edge
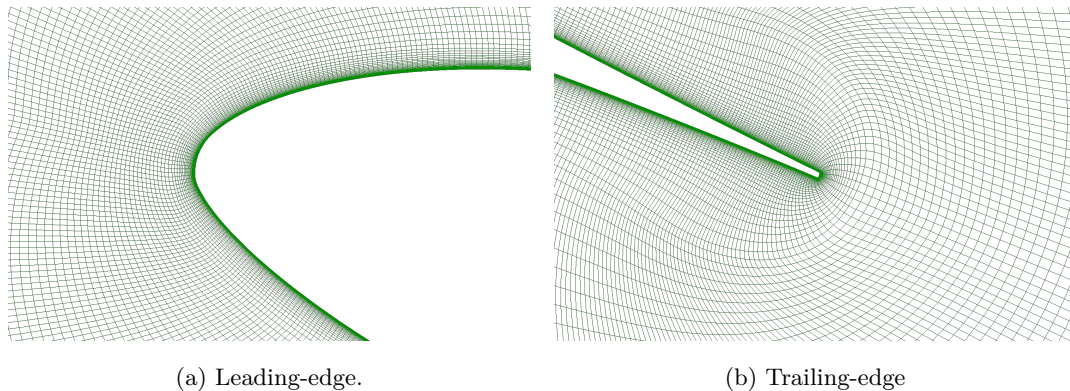
Figure 2. Leading-edge and trailing-edge details of the structured computational mesh of the FFA-W3-211 airfoil with 42.7 M cells. This mesh was chosen for the dynamic simulation.

In Fig. 3, the resulting lift coefficients for the investigated mesh resolutions are visualized. Statistical convergence is monitored as in Ries et al. (2018) and the error bars represent the remaining ensemble error after carrying out the simulations for a non-dimensional time of $t^* = 57$. It can be seen that the results asymptotically approach a lift coefficient of ≈ 1.56. The parameters of the grid convergence study according to Celik et al. (2008) are listed in Tab. 4 and indicate that the mesh with 42.7 M cells is sufficient to predict the lift of separated flow at a Reynolds number of 15 M (GCI = 1.5%). This mesh is, therefore, chosen for the dynamic case.
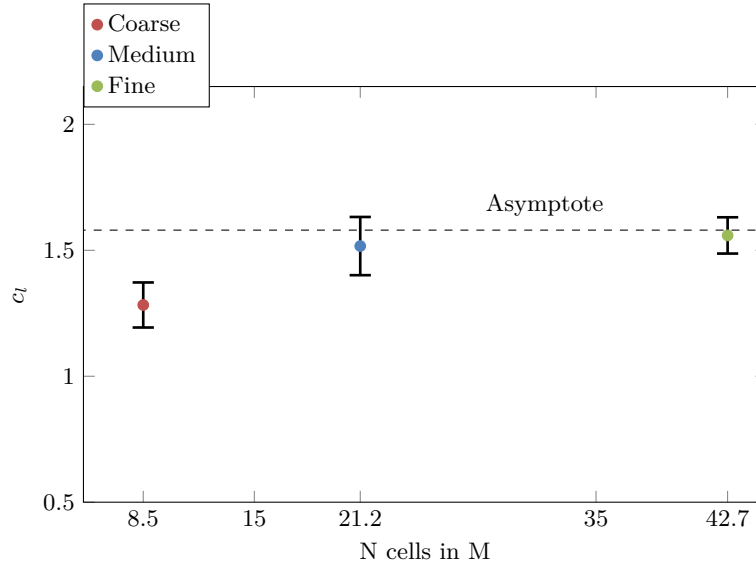
Figure 3. Lift coefficient calculated with DDES and a coarse, medium, and fine mesh resolution at Re = 15 M and angle of attack $\alpha = 20°$. The error bars are the sampling errors calculated as in Ries et al. (2018).

Table 4. Grid convergence study over 3 grids. $c_{l,\text{extrapolated}}$ is the extrapolated c_l assuming ideal mesh refinement. N_{cells} is the number of grid elements and r the refinement ration between two successive grids. GCI is the grid convergence index in percent and its asymptotic value is provided by $GCI_{asymptotic}$, where a value close to unity indicates a grid independent solution. The order achieved in the simulation is given by p.

	c_l	N_{cells}	r	GCI	$GCI_{asymptotic}$	p	$c_{l,\text{extrapolated}}$
Fine	1.559e+00	42.7 M	1.3	1.50%			
Medium	1.52e+00	21.2 M	1.4	5.23%	1.071	5.07	1.58e+00
Coarse	1.28e+00	8.5 M	-	-			

3.2 Dynamic Stall

220 The dynamic case was simulated at Re = 15 M and the pitching angle is defined by

$$\alpha(t) = \bar{\alpha} - \hat{\alpha} \cdot sin(2\pi f_{\mathrm{p}} t) \tag{5}$$

with $\bar{\alpha} = 20°, \hat{\alpha} = 5°$, and $f_{\mathrm{p}} = 1$, which corresponds to a reduced frequency of $k = \frac{\pi \cdot f_{\mathrm{p}} \cdot c}{U_\infty} = 0.137$. Mulleners et al. (2012) introduced the normalized instantaneous effective unsteadiness $\dot{\alpha}_{\mathrm{ss}}^* = \frac{\dot{\alpha}_{\mathrm{ss}} c}{U_\infty}$, which is a measure of the reduced pitching frequency in the moment of exceeding α_{SS}. With $\alpha_{SS} = 18°$, the instantaneous effective unsteadiness calcu-

225 lates to $\dot{\alpha}_{\mathrm{ss}}^* = 0.4$. The chosen time step of the simulation is $\Delta t = 1e^{-5}$, which corresponds to a sampling frequency of

$1e^5$ Hz. The results from the static simulation were used as a start solution for the dynamic case to bridge the initial transient. Three dynamic stall cycles were simulated, which required computational resources of $\approx 1.5e^6$ CPUh. The visualized results are phase-averaged over the last two cycles to bridge the initial transient and the bars are the minimum and maximum values of these cycles. In Fig. 4, the lift hysteresis of the DDES simulation and, for verification, of the BEM simulation are visualized. The angles that mark the stages of the dynamic stall event are plotted on the x-axis.

The lift coefficient increases linearly for $15° < \alpha < 18°$ during the up-stroke. When exceeding α_{SS}, the flow enters the primary instability stage, which increases the lift slope and the lift rises until the maximum of $c_{l,\ max} = 1.8$ at $\approx 20°$. Subsequently, the lift starts oscillating with a local maximum at α_* of $c_l = 1.65$. At this point, the flow enters the vortex formation stage and the dynamic stall vortex is being formed at mid-chord. The vortex is pinched off at α_{DS}, which leads to a sudden breakdown of the lift coefficient and the airfoil enters into deep stall. The lift keeps decreasing during the down-stroke until the global minimum of $c_{l,\ min} = 0.53$ is reached. After that the lift increases until α_{SS} where the flow is fully reattached again.
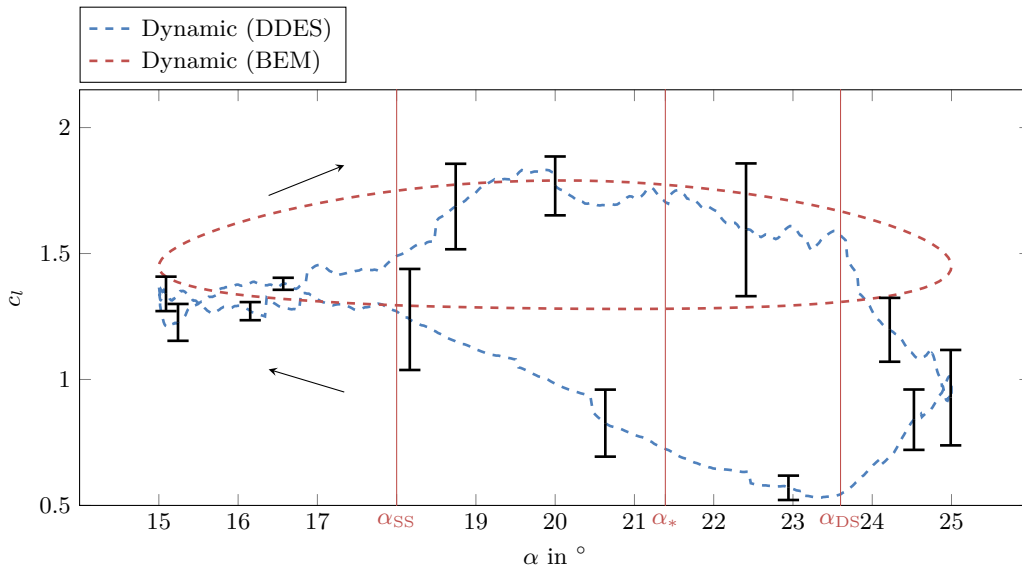
Figure 4. Phase averaged lift coefficient for the DDES (blue) and BEM (red) simulation. The arrows point in the direction of the pitching motion.

The transition between the primary instability phase and the vortex formation stage was determined as in Deparday and Mulleners (2019) with the evolution of the shear layer height Δz^*. The shear layer is located at $U = 0.99 \cdot U_\infty$ and the distance between that layer and the chord of the airfoil is visualized in Fig. 5a.

It can be seen that after exceeding t_*^* the growth rate of Δz^* is 10 times higher than during the primary instability phase. The intersection point between these slopes is the transition point between the primary instability phase and
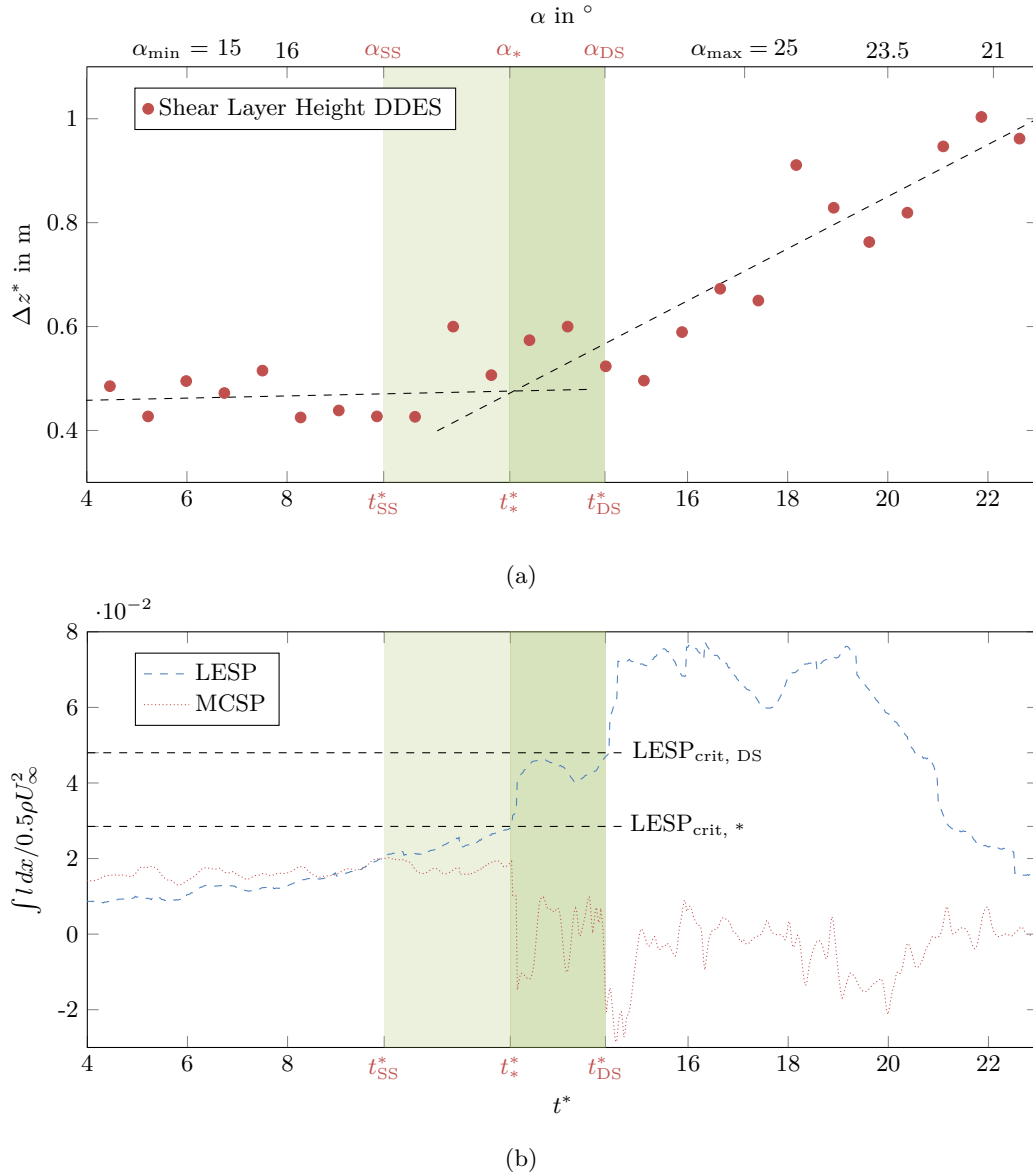
Figure 5. Temporal evolution of the shear layer height simulated with DDES (a). Phase averaged LESP and MCSP. The LESP was obtained by integrating c_p at the wall of the airfoil for $0 < x/c < 0.1$ and the MCSP for $0.45 < x/c < 0.55$ (b).

the vortex formation stage. The angle of static stall is exceeded at $t^*_{\mathrm{SS}} = 9.93$ and the dynamic stall vortex is

245   pinched off at $t^*_{\mathrm{DS}} = 14.35$. This corresponds to the angles of attack of $\alpha_{SS} = 18°$ and $\alpha_{DS} = 23.6°$. The shear layer starts rolling up at $t^*_* = 12.45$ ($\alpha_* = 21.39°$) and the dynamic stall vortex is formed. This means that $\Delta t^*_1 = 2.52$ of the stall delay is attributed to the primary instability stage and $\Delta t^*_2 = 1.9$ to the vortex formation stage. This is

consistent with the observations in Mulleners et al. (2012) and Deparday and Mulleners (2019) that $\Delta t_1^* > \Delta t_2^*$. For the NACA0021 airfoil (t/c = 0.21), Kiefer et al. (2022) introduced the equation

$$t_{\text{DS}}^* - t_{\text{SS}}^* = \frac{A}{k} + f(\beta) \tag{6}$$

250

with A being a constant that is dependent on the airfoil geometry. A/k is the stall delay attributed to the primary instability stage and $f(\beta)$ the stall delay attributed to the vortex formation stage. They found that $A_{\text{NACA0021}} = \pi/20$. In this work, $k = 0.137$, which leads to $A_{\text{FFA-W3-211}} \approx \pi/9$. The airfoils are visualized in 6 and the most noticable differences between them are the camber distribution and the location of the maximum thickness. The

255 NACA0021 has a maximum camber of zero while the FFA-W3-211 has a maximum camber of 0.02 at x/c=0.7. This demonstrates the dependency of the duration of the primary instability stage on the airfoil geometry.
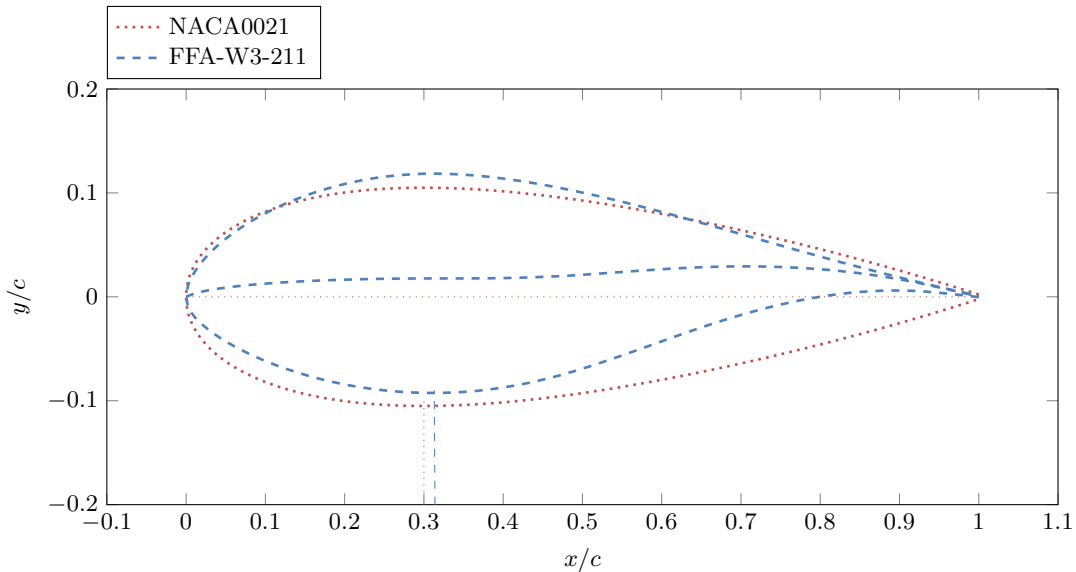
Figure 6. Geometry and camber line of the NACA0021 (red, dotted) and the FFA-W3-211 (blue, dashed) airfoil. The location of the maximum thicknesses are marked on the x-axis.

To enhance current airfoil design processes, Δt_1^* has to be predicted by reduced-order models. The BEM method does not consider the splitting of the stall development stages, which is why a novel criterion that indicates the onset of the vortex formation stage is needed. For thin airfoils, Ramesh et al. (2014) have developed the LESP,

260 which allows for the prediction of the onset of the vortex formation stage with reduced-order models that calculate a transient pressure distribution around the leading-edge of the airfoil. During a dynamic stall cycle of a thin airfoil (t/c < 0.21), the LESP has a maximum of $\text{LESP}_{\text{crit}}$ at t_*^* and breaks down subsequently. The temporal evolution of the LESP for the DDES simulation in this work is visualized in Fig. 5a and the transition points between the

stages of dynamic stall are marked on the x-axis. The primary instability phase is colored in light green and the
vortex formation stage in darker green. The LESP increases quadratically during the up-stroke of the airfoil and
spikes at $t^*_{SS} = 12.45$ instead of breaking down as in Deparday and Mulleners (2019) because the leading-edge flow
stays attached during the dynamic stall cycle. The LESP subsequently decreases and spikes again at $t^*_{SS} = 12.35$.
During the deep stall stage, it reaches a maximum of $\approx 7.8e^{-2}$ and starts decreasing at $t^* = 19.5$. It is striking, that
the temporal evolution of the LESP indicates both the onset of the vortex formation stage and the onset of dynamic
stall by a sudden increase in magnitude. The transition of the primary instability stage to the vortex formation
stage happens when exceeding $\text{LESP}_{\text{crit}, *} = 2.85e^{-2}$ and the dynamic stall vortex is pinched off after exceeding
$\text{LESP}_{\text{crit, DS}} = 4.8e^{-2}$.

Since the dynamic stall vortex both forms and detaches at mid-chord, the LESP is an indirect way of monitoring
the stages of dynamic stall. We, therefore, introduce the MCSP, which is a modified version of the LESP. Instead of
integrating the lift at the leading-edge, the MCSP is calculated by integrating the lift between $0.45 < \text{x/c} < 0.55$,
which is where the flow detaches. During the up-stroke of the airfoil, the MCSP remains almost constant at $1.8e^{-2}$
and intersects the LESP at t^*_{SS}. As expected, it drops massively at t^*_* and t^*_{DS}, which indicates the onset of the
vortex formation stage and deep stall.

Both separation criteria indicate the onset of the stages of dynamic stall. The MCSP seems to be the more robust
criterion because it monitors the pressure distribution in the region where the flow detaches. Future work should
investigate the sensitivity of the airfoil's camber distribution and the location of the maximum thickness. A correlation
of the temporal evolution of the MCSP and these airfoil parameters would allow for the development of a reduced-
order model that can predict the onset of the vortex formation stage.

4   Conclusions

Wind turbines operate in highly unsteady wind conditions, which makes avoiding dynamic stall entirely an impos-
sible task. In order to design airfoils that are less prone to dynamic stall, a reduced-order model that can predict
the onset of the formation of the dynamic stall vortex is required. The research presented here contributes to the
development of such a reduced-order model for thick wind turbine airfoils (t/c > 0.21) by analyzing a conducted
Delayed Detached-Eddy simulation of a pitching FFA-W3-211 airfoil at Re = 15 M.

The dynamic time scales were obtained by monitoring the transient shear layer height. We found that the growth
rate of the shear layer height increases ten-fold during the transition between the primary instability and the vortex
formation stage. Comparing the stall delays attributed to these stages with the results of Kiefer et al. (2022), demon-
strates a massive dependency of the stall delay towards the camber distribution and the location of the maximum
thickness of an airfoil.

The Leading-Edge Suction-Parameter (LESP), introduced by Ramesh et al. (2014) for predicting the onset of the
vortex formation stage on thin airfoils, was analyzed to test its feasibility for thick thick airfoils. It was found that

the temporal evolution of the LESP indicates the onset of the vortex formation stage and deep stall, even though the flow at the leading-edge remains attached during the dynamic stall cycle. For airfoils as they occur on wind turbines, the dynamic stall vortex forms and pinches off at mid-chord, which illustrates that monitoring the LESP
300   is an indirect way of predicting the onset of the vortex formation stage. Therefore, we introduced the Mid-Chord Suction-Parameter (MCSP), which is a modified version of the LESP. Since the MCSP is based on the pressure distribution at the location of the flow separation, it seems to be more robust for the application to thick airfoils compared to the LESP. Analogous to the LESP, the MCSP indicates the transition points of the dynamic stall stages.

305   Future work should investigate the sensitivity of the airfoil camber distribution and the location of the maximum thickness to the stall delay attributed to the primary instability phase Δt_1^*. Establishing correlations between $\text{LESP}_{\text{crit}}$, the temporal evolution of MCSP, and these airfoil parameters would allow for the development of a reduced-order model that can predict the dynamic time scales in the design process of new airfoil geometries.

Author contributions. AGY conducted the DDES simulations and provided the figures and tables in the Methodology chapter.
310   JAP conducted the BEM simulation and wrote the Methodology chapter. JDA evaluated the results of the simulations and wrote the remaining chapters of the paper. All three worked under the supervision and review of JRS and LW.

Competing interests. The authors declare that they have no conflict of interest.

Acknowledgements. The authors gratefully acknowledge the computing time granted by the Resource Allocation Board and provided on the supercomputer Lise and Emmy at NHR@ZIB and NHR@Göttingen as part of the NHR infrastructure. The
315   calculations for this research were conducted with computing resources under the project nii00172. The authors thank the cluster system at the Leibniz Universität of Hannover for the HPC resources, which have contributed to the development of the research results presented here. The present work has been carried out in the subproject A02 within the Collaborative Research Center (CRC) 1463 "Integrated design and operation methodology for offshore megastructures" which is funded by the Deutsche Forschungsgemeinschaft (DFG, German Research Foundation). The authors thank the DFG for the support.

References

Ahrens, J. D., Ziesse, M., Wein, L., and Seume, J. R.: A Novel And Costeffective Approach To Simulating Dynamic Stall On Rotating Wind Turbine Blades With A Changing Angle Of Attack, GPPS Chania, 2022.

Andersen, P. B., Gaunaa, M., Bak, C., and Hansen, M. H.: A dynamic stall model for airfoils with deformable trailing edges, Wind Energy: An International Journal for Progress and Applications in Wind Power Conversion Technology, 12, 734–751, 2009.

Bangga, G., Weihing, P., Lutz, T., and Krämer, E.: Effect of computational grid on accurate prediction of a wind turbine rotor using delayed detached-eddy simulations, Journal of Mechanical Science and Technology, 31, 2359–2364, 2017.

Bertagnolio, F., Sørensen, N., Johansen, J., and Fuglsang, P.: Wind turbine airfoil catalogue, 2001.

Betz, A.: Wind-energie und ihre ausnutzung durch windmühlen, vol. 2, Vandenhoeck & Ruprecht, 1926.

Branlard, E., Jonkman, B., Pirrung, G. R., Dixon, K., and Jonkman, J.: Dynamic inflow and unsteady aerodynamics models for modal and stability analyses in OpenFAST, Journal of Physics: Conference Series, 2265, 032 044, https://doi.org/10.1088/1742-6596/2265/3/032044, 2022.

Brunner, C. E., Kiefer, J., Hansen, M. O., and Hultmark, M.: Study of Reynolds number effects on the aerodynamics of a moderately thick airfoil using a high-pressure wind tunnel, Experiments in Fluids, 62, 1–17, 2021.

Celik, I. B., Ghia, U., Roache, P. J., and Freitas, C. J.: Procedure for estimation and reporting of uncertainty due to discretization in CFD applications, Journal of fluids Engineering-Transactions of the ASME, 130, 2008.

Corke, T. C. and Thomas, F. O.: Dynamic stall in pitching airfoils: aerodynamic damping and compressibility effects, Annual Review of Fluid Mechanics, 47, 479–505, 2015.

Deparday, J. and Mulleners, K.: Modeling the interplay between the shear layer and leading edge suction during dynamic stall, Physics of Fluids, 31, 107 104, 2019.

Gerontakos, P. and Lee, T.: Dynamic stall flow control via a trailing-edge flap, AIAA journal, 44, 469–480, 2006.

Glauert, H.: A general theory of the autogyro, Tech. rep., HM Stationery Office, 1926.

Glauert, H.: Airplane Propellers, pp. 169–360, Springer Berlin Heidelberg, Berlin, Heidelberg, https://doi.org/10.1007/978-3-642-91487-4_3, 1935.

Gupta, R. and Ansell, P. J.: Unsteady flow physics of airfoil dynamic stall, AIAA journal, 57, 165–175, 2019.

Gupta, S. and Leishman, J. G.: Dynamic stall modelling of the S809 aerofoil and comparison with experiments, Wind Energy: An International Journal for Progress and Applications in Wind Power Conversion Technology, 9, 521–547, 2006.

Huang, X., Albers, M., Meysonnat, P., Meinke, M., and Schröder, W.: Analysis of the effect of freestream turbulence on dynamic stall of wind turbine blades, International Journal of Heat and Fluid Flow, 85, 108 668, 2020.

Issa, R. I.: Solution of the implicitly discretised fluid flow equations by operator-splitting, Journal of computational physics, 62, 40–65, 1986.

Jasak, H.: Dynamic Mesh Handling in OpenFOAM, American Institute of Aeronautics and Astronautics, https://doi.org/10.2514/6.2009-341, 2009.

Khan, M. A.: Dynamic stall modeling for wind turbines, 2018.

Kiefer, J., Brunner, C. E., Hansen, M. O., and Hultmark, M.: Dynamic stall at high Reynolds numbers induced by ramp-type pitching motions, Journal of Fluid Mechanics, 938, 2022.

Konstadinopoulos, P., Thrasher, D., Mook, D., Nayfeh, A., and Watson, L.: A vortex-lattice method for general, unsteady aerodynamics, Journal of aircraft, 22, 43–49, 1985.

Leishman, G. J.: Principles of helicopter aerodynamics, Cambridge university press, 2006.

360 Leishman, J. G. and Beddoes, T.: A Semi-Empirical model for dynamic stall, Journal of the American Helicopter society, 34, 3–17, 1989.

Letzgus, J., Gardner, A. D., Schwermer, T., Keßler, M., and Krämer, E.: Numerical investigations of dynamic stall on a rotor with cyclic pitch control, Journal of the American Helicopter Society, 64, 1–14, 2019.

Merz, C. B., Wolf, C., Richter, K., Kaufmann, K., Mielke, A., and Raffel, M.: Spanwise differences in static and dynamic stall on a pitching rotor blade tip model, Journal of the American Helicopter Society, 62, 1–11, 2017.

Mulleners, K., Le Pape, A., Heine, B., and Raffel, M.: The dynamics of static stall, Experiments in Fluids, 52, 779–793, 2012.

Pitt, D. M. and Peters, D. A.: Theoretical prediction of dynamic-inflow derivatives, 1980.

Prandtl, L. and Betz, A.: Vier Abhandlungen zur Hydrodynamik und Aerodynamik, Göttinger Klassiker der Strömungsmechanik, Univ.-Verlag Göttingen, https://books.google.de/books?id=_mpG5-KWaN0C, 2010.

370 Ramesh, K., Gopalarathnam, A., Granlund, K., Ol, M. V., and Edwards, J. R.: Discrete-vortex method with novel shedding criterion for unsteady aerofoil flows with intermittent leading-edge vortex shedding, Journal of Fluid Mechanics, 751, 500–538, 2014.

Ries, F., Nishad, K., Dressler, L., Janicka, J., and Sadiki, A.: Evaluating large eddy simulation results based on error analysis, Theoretical and Computational Fluid Dynamics, 32, 733–752, 2018.

375 Schwermer, T., Gardner, A. D., and Raffel, M.: A novel experiment to understand the dynamic stall phenomenon in rotor axial flight, Journal of the American Helicopter Society, 64, 1–11, 2019.

Sharma, A. and Visbal, M.: Numerical investigation of the effect of airfoil thickness on onset of dynamic stall, Journal of Fluid Mechanics, 870, 870–900, 2019.

Simms, D., Schreck, S., Hand, M., and Fingersh, L. J.: NREL unsteady aerodynamics experiment in the NASA-Ames wind tunnel: a comparison of predictions to measurements, Tech. rep., National Renewable Energy Lab.(NREL), Golden, CO (United States), 2001.

Solomin, E. V. and Ryavkin, G. N.: Horizontal Axis Wind Turbine Weather Vane Aerodynamic Characteristics: Delayed Detached Eddy Simulation and Experimental Approach, Mathematics, 11, 1834, 2023.

Steffen, r, C., Reddy, D., and Zaman, K.: Analysis of flowfield from a rectangular nozzle with delta tabs, in: Fluid Dynamics Conference, p. 2146, 1995.

Tangler, J. L.: Nebulous Art of Using Wind-Tunnel Airfoil Data for Predicting Rotor Performance- Preprint, 2002., 2002.

Theodorsen, T.: General theory of aerodynamic instability and the mechanism of flup., NACA, 1935.

van Bussel, G. J. W.: History of Aerodynamic Modelling, pp. 1–54, Springer International Publishing, Cham, https://doi.org/10.1007/978-3-030-05455-7_9-1, 2020.

390 Yalcin, , Cengiz, K., Wein, L., Özyörük, Y., and Seume, J. R.: Transitional DDES Study over a Circular Cylinder and an Airfoil Profile, The 13th International ERCOFTAC symposium on engineering, turbulence, modelling and measurements, 2021.